Supporting Information for

Functional modified separator with high-entropy material for high performance Zn-I_2 batteries

Hongfeng Jia[a], Yanxin Li[a], Yuehan Hao[a], Xinyuan Hu[a], Usman Ali[a], Bingqiu Liu[a], Lu Li[a], Lingyu Zhang[a]*, Sun Hang[b], and Chungang Wang[a]*

[a] Department of Chemistry, Northeast Normal University, 5268 Renmin Street, Changchun, Jilin 130024, P. R. China

[b] Jilin Institute of Metrology Science-Jilin Key Laboratory of Metrology and Testing Instruments and Technology, No. 2699 Yiju Road, Changchun, Jilin 130024, P. R. China

*Corresponding author. E-mail: zhaoliang@nenu.edu.cn; wangcg925@nenu.edu.cn

Experimental section

Materials:

Ytterbium (III) chloride hexahydrate ($YbCl_3 \cdot 6H_2O$, 99.99%), yttrium (III) chloride hexahydrate ($YCl_3 \cdot 6H_2O$, 99.99%), indium chloride hydrate ($InCl_3 \cdot 6H_2O$, 99.99%), thulium chloride hexahydrate ($TmCl_3 \cdot 6H_2O$, 99.99%), and Zn foils (99.99%) were obtained from Energy Chemical. Zirconium (IV) chloride ($ZrCl_4$, 99.5%) was bought from Strem Chemicals, Inc. Zinc sulfate was purchased from Sigma-Aldrich. All reagents were used directly without further purification. Deionized (DI) water was thoroughly used during the experiment.

Preparation of CNFs/HEO:

Equivalent stoichiometric amounts of $YbCl_3 \cdot 6H_2O$, $YCl_3 \cdot 6H_2O$, $InCl_3 \cdot 6H_2O$, $TmCl_3 \cdot 6H_2O$, and $ZrCl_4$ were dissolved in 7 mL DMF in turn. Subsequently, 500 mg PAN was added, and the mixture was stirred at 50°C for 10 h to make sure the complete dissolution of each component. Electrospinning was conducted by TEADFS-100 (Beijing Technova Technology Co., Ltd.). The flow rate of the spinning solution was 0.013 mL/min and collected by aluminum foil fixed on a grounded steel drum. The as-prepared fibers were placed in an oven at 80 °C for 12 h until DMF was completely removed. The fibers were first stabilized at 220°C for 2 h and then heated to 900°C for 2 h with a heating rate of 2°C/min in an Ar atmosphere. The as-prepared material was named as CNFs/HEO.

Preparation of CNFs/Yb_2O_3:

1.5 mmol $YbCl_3 \cdot 6H_2O$ was added to 7 mL DMF with continuous stirring. After

complete dissolution, 500 mg PAN was added. The mixed solution was stirred at 50°C for 10 h. The electrospinning procedure and parameter were identical to the CNFs/HEO.

Synthesis of the cathode and battery Assembly:

Firstly, activated carbon were mixed and ground in a mortar with iodine in a mass ratio of 1:1.2. Then, the mixture was transferred into a glass tube and thermally sealed. After heating at 120 °C for 6 h, the powder was collected and ground in a mortar with acetylene black, CMC, and SBR in a mass ratio of 7:2:0.5:0.5. Then, the mixture was applied to the carbon cloth. The cathode was dried in a vacuum oven at 30 °C for 6 h. The active material (I_2) loading of the individual electrode was about 1.0-1.2 mg cm^{-2}. CNFs/Yb_2O_3 and CNFs/HEO were used as the cathode-modified interface and assembled between the cathode and the separator. 120 μL of 2 M $ZnSO_4$ was selected as an electrolyte.

Electrochemical measurements:

The electrochemical impedance spectroscopy (EIS) was collected over the frequency range from 100 kHz to 0.1 Hz. Cyclic voltammetry (CV) was tested on the CHI760E electrochemical workstation with a voltage range between 0.6 and 1.6 V at a scan rate of 0.5 mV s^{-1}. The discharge-charge cycling of Zn-I_2 was measured on the Neware battery test system (CT-ZWJ-4'S-T-1U, Shenzhen, China) and LAND battery test instrument (CT2001A, LAND, China) within a voltage range of 0.6-1.6 V.

Materials characterization:

X-ray powder diffraction (XRD) analysis was obtained on a D8 Focus diffractometer

(Bruker) with Cu-Ka radiation (λ=0.15405 nm) from Rigaku Corporation in Japan. High-resolution transmission electron microscope (HR-TEM) characterizations were taken by JEOLJEM-2100F transmission electron microscope at 200 kV accelerating voltage. Scanning electron microscopy (SEM) images were measured by HITACHI SU8010 field-emission scanning electron microscope (FEI Co.) with an energy-dispersive X-ray spectrum (EDS) from the Hitachi Limited in Japan. Raman spectrum was recorded at room temperature with a JY HR-800 LabRam confocal Raman microscope in a backscattering configuration with an excitation wavelength of 488 nm. X-ray photoelectron spectrum (XPS) was tested on an ECSALAB 250 using non-monochromatized Al-Kα radiation. An atom force microscope (AFM) was performed on Asylum Research Cypher ES.

DFT calculations:

First-principles calculations are performed in the framework of Density Functional Theory (DFT), which is implemented in the Vienna Ab initio simulation package (VASP)[1,2]. The projector augmented wave (PAW)[3] potential was used with a plane-wave cutoff energy of 500 eV. Conjugate gradient method was used for geometric optimization, with the convergence threshold set at 10^{-6} eV per atom in energy and 0.01 eV·Å^{-1} in force. A vacuum distance of >15 Å was employed to avoid interactions of neighboring images. The DFT-D3 method including vdW is used to deal with the inter-layer van der Waals forces[4]. Considering the strong correlation of transition metals, the density of states (DOS) was calculated by the GGA+U method[5].

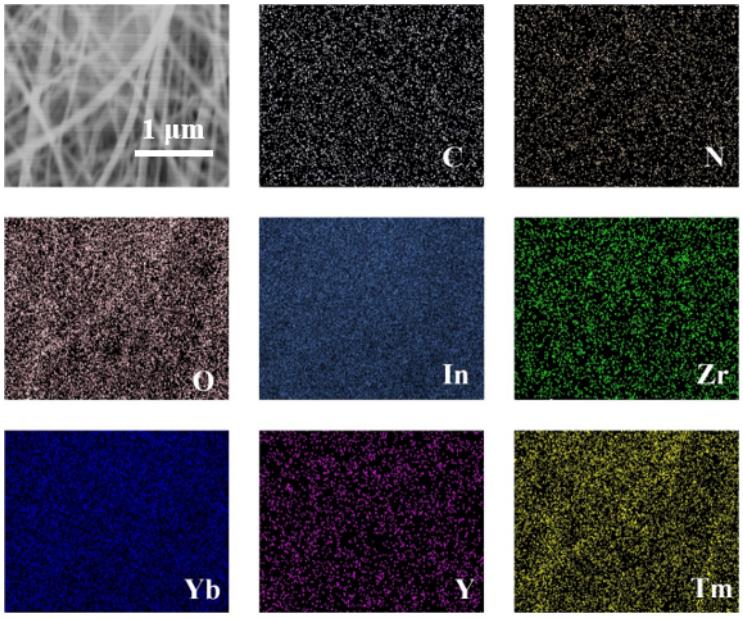

Fig. S1 SEM images and corresponding mapping analysis of CNFs/HEO.

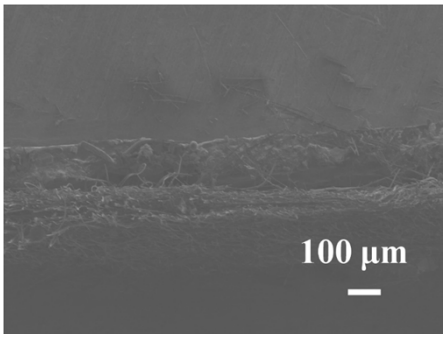

Fig. S2 Cross-section SEM image of CNFs/HEO.

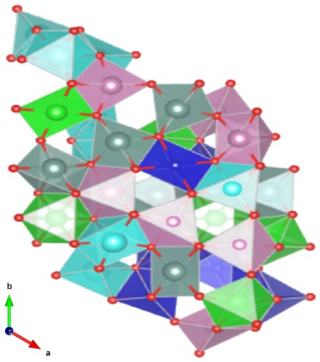

Fig. S3 Crystal structure of HEO.

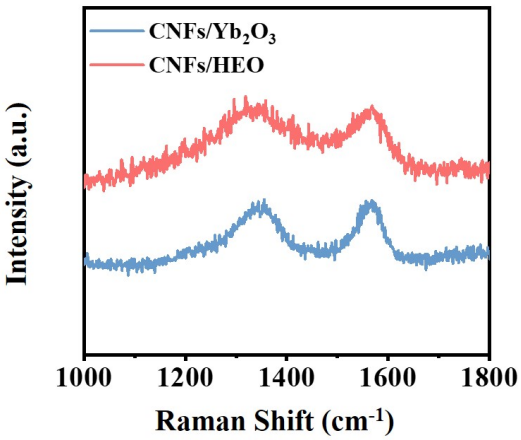

Fig. S4 Raman spectra of CNFs/Yb_2O_3 and CNFs/HEO.

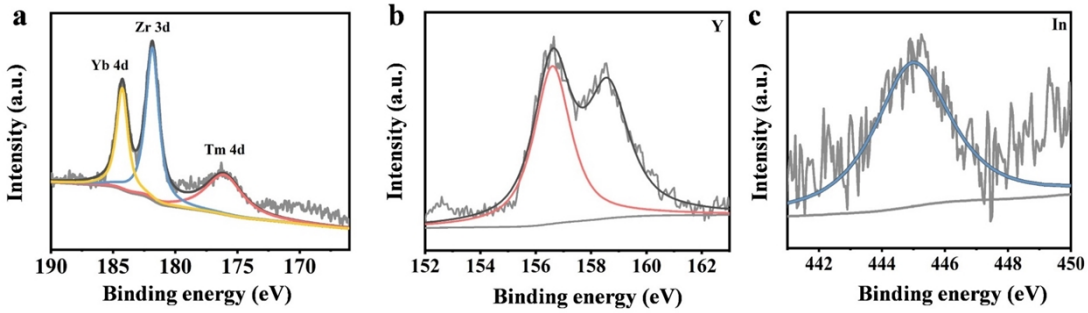

Fig. S5 XPS spectra of (a) Yb, Zr, and Tm, (b) Y, and (c) In in CNFs/HEO.

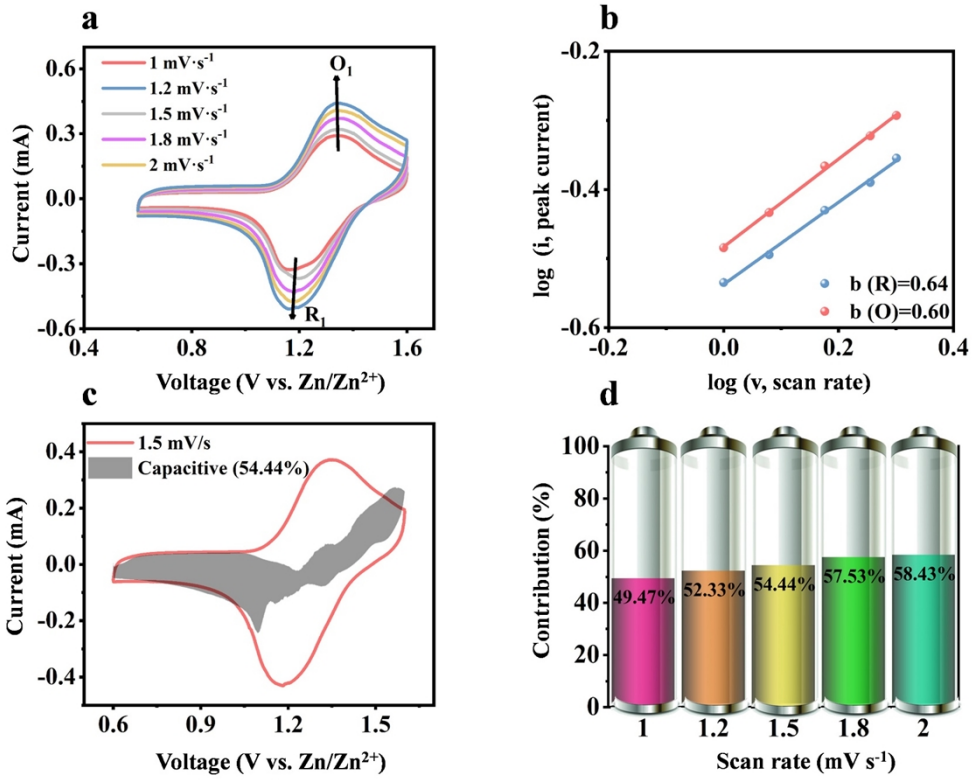

Fig. S6 (a) CV curves at different scan rates, (b) Log (i) -log (v) plots for specific peak current, (c) Capacitive contribution at 1.5 mV s^{-1}, and (d) Capacitive and diffusion contribution versus scan rate curve of CNFs/Yb_2O_3.

Generally speaking, the peak current (i) and scan rate (v) maintain a functional relationship as follows:

$$i = av^b \quad (1)$$

where a and b represent arbitrary coefficients[6,7]. When the b value is close to 0.5, the electrochemical kinetics is denoted by the diffusion process caused by zinc ion (de)-intercalation. When b is closer to 1.0, it demonstrates that a surface redox reaction dominates the capacitive behavior. While the value of b is between 0.5 and 1.0, it means the electrochemical kinetics is determined by both the diffusion process of Zn^{2+} and the capacitive behavior. Additionally, according to

$$i = k_1v + k_2v^{1/2} \quad (2)$$

the specific contributions of the capacitive behavior (k_1v) and the diffusion-controlled insertion ($k_2v^{1/2}$) at different scan rates were calculated[8,9].

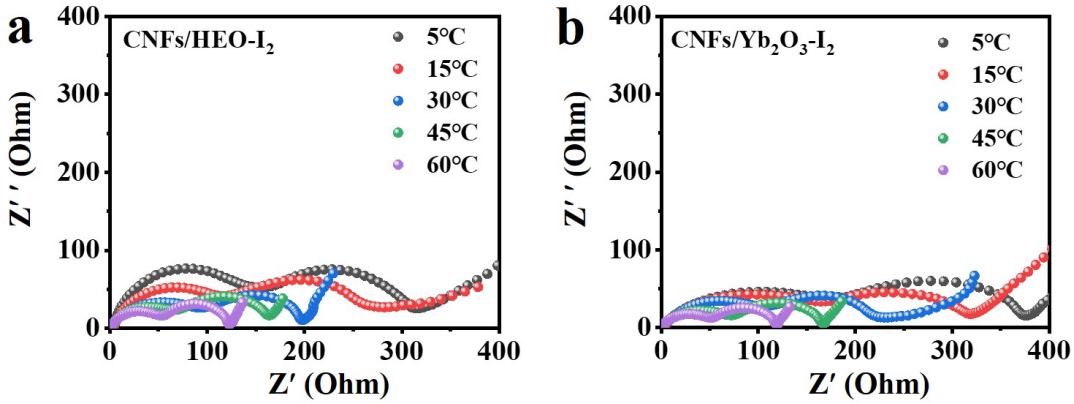

Fig. S7 Arrhenius activation energy (E_a) of (a) CNFs/HEO and (b) CNFs/Yb_2O_3 batteries.

Ea of the I_2 reduction process can be calculated according to the following Arrhenius equation:

$$1/Rct = Aexp(-Ea/RT)$$

Where Rct, A, R, and T represent the charge-transfer resistance, frequency factor, gas constant, and absolute temperature, respectively. EIS profiles of the four electrodes at different temperatures from 5 to 60 ºC were tested.

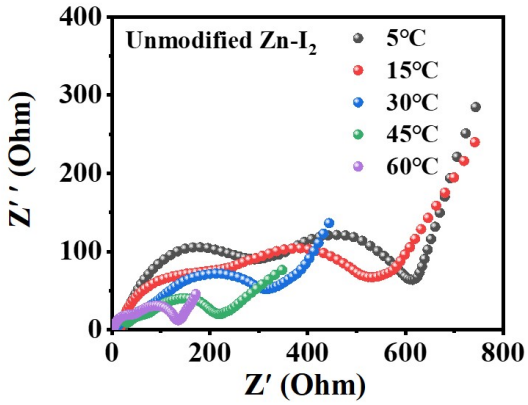

Fig. S8 Arrhenius activation energy (E_a) of unmodified Zn-I_2 batteries.

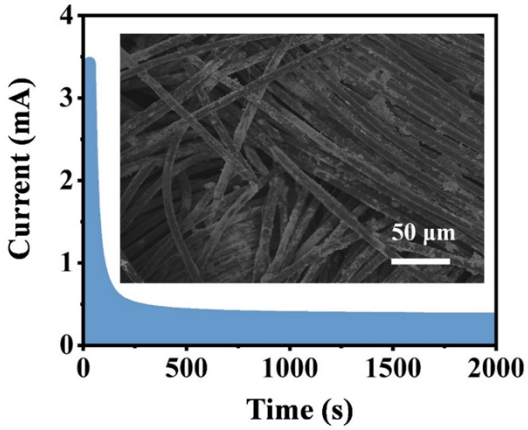

Fig. S9 Potentiostatic deposition curves of I_2 on the cathode with CNFs/Yb_2O_3 (The inset reflects the surface state after iodine deposition).

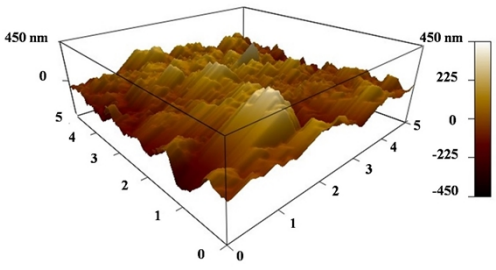

Fig. S10 AFM image of the cathode with CNFs/Yb_2O_3 modified layer after depositing I_2.

1

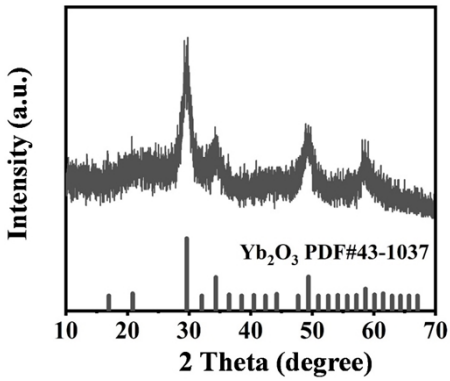

2

3 Fig. S11 XRD pattern of CNFs/HEO after cycling 1000 cycles.

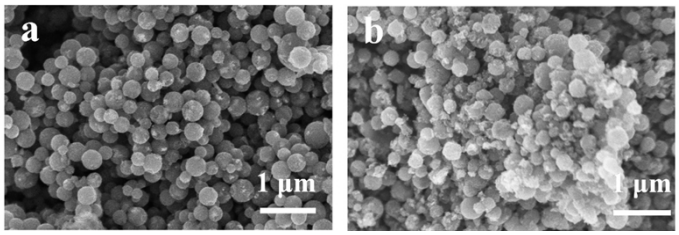

Fig. S12 SEM images of (a) OMMC NSs and (b) OMMC-I_2 NSs.

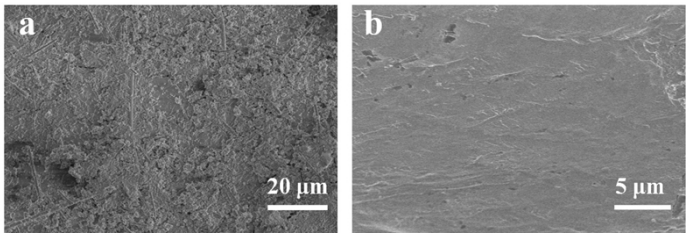

Fig. S13 SEM images of the zinc anodes after cycling in the (a) CNFs/Yb_2O_3 and (b) CNFs/HEO batteries.

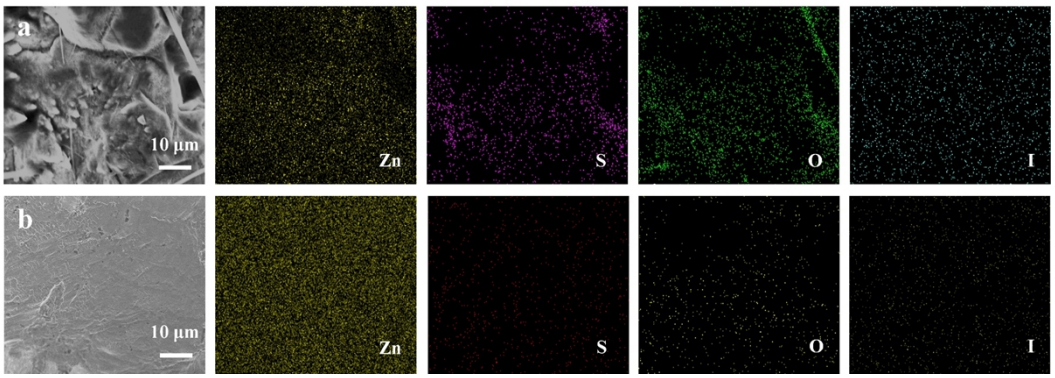

Fig. S14 SEM images and corresponding mapping analysis of the zinc anodes after cycling in the (a) CNFs/Yb_2O_3 and (b) CNFs/HEO batteries.

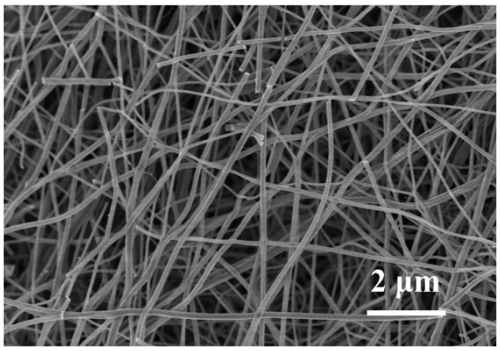

Fig. S15 SEM image of CNFs/HEO after cycling.

Table S1. The refined crystallographic data of HEO obtained from XRD Rietveld refinements.

Sample	a (=b=c)/Å	Volume/Å^3
HEO	10.41	1128.11

Table S2. Comparison of main parameters and cycling property for this work with previous works.

Electrode	Current density (A g^{-1})	Cycling life (h)	Capacity retention (%)	Ref
eIM	6	23000	80	[10]
NHPC	5	10000	90.6	[11]

PNC-1000	1	10000	89	[12]
I_2@GP-CMT	4	1000	88.8	[13]
NPCNFs-800	2	6000	99.4	[14]
$Co[Co_{1/4}Fe_{3/4}(CN)_6]/I_2$	4	2000	80.2	[15]
I_2/OSTC	1	10000	85.0	[16]
CNFs/HEO	**10**	**30000**	**62.5**	**This work**

References

1. G. Kresse and J. Furthmüller, Efficient iterative schemes for ab initio total-energy calculations using a plane-wave basis set, *Phys. Rev. B*, 1996, **54**, 11169-11186.

2. G. Kresse and J. Hafner, Ab initio molecular dynamics for open-shell transition metals, *Phys. Rev. B*, 1993, **48**, 13115-13118.

3. P. E. Blöchl, Projector augmented-wave method, *Phys. Rev. B*, 1994, **50**, 17953-17979.

4. S. Grimme, J. Antony, S. Ehrlich and H. Krieg, A consistent and accurate ab initio parametrization of density functional dispersion correction (DFT-D) for the 94 elements H-Pu, *J. of Chem. Phys.*, 2010, **132**. https://doi.org/10.1063/1.3382344.

5. M. Liu, Z. Rong, R. Malik, P. Canepa, A. Jain, G. Ceder and K. A. Persson, Spinel compounds as multivalent battery cathodes: a systematic evaluation based on ab initio calculations, *Energy Environ. Sci.*, 2015, **8**, 964-974.

6. J. Wang, J. Polleux, J. Lim and B. Dunn, Pseudocapacitive contributions to electrochemical energy storage in TiO_2 (anatase) nanoparticles, *J. Phys. Chem. C*, 2007, **111**, 14925-14931.

7. V. Augustyn, J. Come, M. A. Lowe, J. W. Kim, P.-L. Taberna, S. H. Tolbert, H. D. Abruña, P. Simon and B. Dunn, High-rate electrochemical energy storage through Li^+

intercalation pseudocapacitance, *Nat. Mater.*, 2013, **12**, 518-522.

8. F. Wan, L. Zhang, X. Dai, X. Wang, Z. Niu and J. Chen, Aqueous rechargeable zinc/sodium vanadate batteries with enhanced performance from simultaneous insertion of dual carriers, *Nat. Commun.*, 2018, **9**. https://doi.org/10.1038/s41467-018-04060-8.

9. V. Augustyn, P. Simon and B. Dunn, Pseudocapacitive oxide materials for high-rate electrochemical energy storage, *Energy Environ. Sci.*, 2014, **7**, 1597-1614.

10. X. Li, N. Li, Z. Huang, Z. Chen, G. Liang, Q. Yang, M. Li, Y. Zhao, L. Ma, B. Dong, Q. Huang, J. Fan and C. Zhi, Enhanced redox kinetics and duration of aqueous I_2/I^- conversion chemistry by MXene confinement, *Adv. Mater.*, 2021, **33**, 2006897.

11. Z. Gong, C. Song, C. Bai, X. Zhao, Z. Luo, G. Qi, X. Liu, C. Wang, Y. Duan and Z. J. S. C. M. Yuan, Anchoring high-mass iodine to nanoporous carbon with large-volume micropores and rich pyridine-N sites for high-energy-density and long-life Zn-I_2 aqueous battery, *Sci. Chi. Mater.*, 2023, **66**, 556-566.

12. T. Liu, H. Wang, C. Lei, Y. Mao, H. Wang, X. He and X. J. E. S. M. Liang, Recognition of the catalytic activities of graphitic N for zinc-iodine batteries, *Energy Storage Mater.*, 2022, **53**, 544-551.

13. S. Chai, J. Yao, Y. Wang, J. Zhu and J. J. C. E. J. Jiang, Mediating iodine cathodes with robust directional halogen bond interactions for highly stable rechargeable Zn-I_2 batteries, *Chem. Eng. J.*, 2022, **439**, 135676.

14. Y. He, M. Liu, S. Chen and J. J. S. C. C. Zhang, Shapeable carbon fiber networks with hierarchical porous structure for high-performance Zn-I_2 batteries, *Sci. Chi. Chem.*, 2022, **65**, 391-398.

15. L. Ma, Y. Ying, S. Chen, Z. Huang, X. Li, H. Huang and C. Zhi, Electrocatalytic iodine reduction reaction enabled by aqueous zinc-iodine battery with improved power and energy densities, *Angew. Chem. Int. Ed.*, 2021, **60**, 3791-3798.

16. M. Chen, W. Zhu, H. Guo, Z. Tian, L. Zhang, J. Wang, T. Liu, F. Lai and J. J. E. S. M. Huang, Tightly confined iodine in surface-oxidized carbon matrix toward dual-mechanism zinc-iodine batteries, *Energy Storage Mater.*, 2023, **59**, 102760.